

An n—n type heterojunction enabling highly efficient carrier separation in inorganic solar cells

Gang Li(李刚), Yuqian Huang(黄玉茜), Rongfeng Tang(唐荣风), Bo Che(车波), Peng Xiao(肖鹏),Weitao Lian(连伟涛), Changfei Zhu(朱长飞), and Tao Chen(陈涛)

Citation: Chin. Phys. B, 2022, 31 (**3**): 038803. DOI: 10.1088/1674-1056/ac4022
Journal homepage: http://cpb.iphy.ac.cn; http://iopscience.iop.org/cpb

What follows is a list of articles you may be interested in

Reveal the large open-circuit voltage deficit of all-inorganic $CsPbIBr_2$ perovskite solar cells

Ying Hu(胡颖), Jiaping Wang(王家平), Peng Zhao(赵鹏), Zhenhua Lin(林珍华), Siyu Zhang(张思玉),Jie Su(苏杰), Miao Zhang(张苗), Jincheng Zhang(张进成), Jingjing Chang(常晶晶), and Yue Hao(郝跃)

Chin. Phys. B, 2022, 31 (**3**): 038804. DOI: 10.1088/1674-1056/ac464b

Effect of net carriers at the interconnection layer in tandem organic solar cells

Li-Jia Chen(陈丽佳), Guo-Xi Niu(牛国玺), Lian-Bin Niu(牛连斌), and Qun-Liang Song(宋群梁)

Chin. Phys. B, 2022, 31 (**3**): 038802. DOI: 10.1088/1674-1056/ac4485

Charge transfer modification of inverted planar perovskite solar cells by NiO_x/Sr: NiO_x bilayer hole transport layer

Qiaopeng Cui(崔翘鹏), Liang Zhao(赵亮), Xuewen Sun(孙学文), Qiannan Yao(姚倩楠), Sheng Huang(黄胜), Lei Zhu(朱磊), Yulong Zhao(赵宇龙), Jian Song(宋健), and Yinghuai Qiang(强颖怀)

Chin. Phys. B, 2022, 31 (**3**): 038801. DOI: 10.1088/1674-1056/ac1fda

High efficiency ETM-free perovskite cell composed of CuSCN and increasing gradient $CH_3NH_3PbI_3$

Tao Wang(汪涛), Gui-Jiang Xiao(肖贵将), Ren Sun(孙韧), Lin-Bao Luo(罗林保), and Mao-Xiang Yi(易茂祥)

Chin. Phys. B, 2022, 31 (**1**): 018801. DOI: 10.1088/1674-1056/ac0bb0

Current improvement in substrate structured Sb_2S_3 solar cells with $MoSe_2$ interlayer

Lu Liu(刘璐), Sheng-Li Zhang(张生利), Jian-Yu Wu(吴建宇), Wei-Huang Wang(王伟煌), Wei Liu(刘玮), Li Wu(武莉), Yi Zhang(张毅)

Chin. Phys. B, 2020, 29 (**5**): 058801. DOI: 10.1088/1674-1056/ab8220

SPECIAL TOPIC — Emerging photovoltaic materials and devices

An n–n type heterojunction enabling highly efficient carrier separation in inorganic solar cells

Gang Li(李刚)[1,2], Yuqian Huang(黄玉茜)[1,2], Rongfeng Tang(唐荣凤)[1,2], Bo Che(车波)[1,2], Peng Xiao(肖鹏)[1,2], Weitao Lian(连伟涛)[1,2], Changfei Zhu(朱长飞)[1,2], and Tao Chen(陈涛)[2,1,†]

[1] *Hefei National Laboratory for Physical Sciences at Microscale, CAS Key Laboratory of Materials for Energy Conversion, Department of Materials Science and Engineering, School of Chemistry and Materials Science, University of Science and Technology of China, Hefei* 230026, *China*

[2] *Institute of Energy, Hefei Comprehensive National Science Center, Hefei* 230026, *China*

(Received 10 October 2021; revised manuscript received 24 November 2021; accepted manuscript online 5 December 2021)

Carrier separation in a solar cell usually relies on the p–n junction. Here we show that an n–n type inorganic semiconductor heterojunction is also able to separate the exciton for efficient solar cell applications. The n–n type heterojunction was formed by hydrothermal deposition of $Sb_2(S,Se)_3$ and thermal evaporation of Sb_2Se_3. We found that the n–n junction is able to enhance the carrier separation by the formation of an electric field, reduce the interfacial recombination and generate optimized band alignment. The device based on this n–n junction shows 2.89% net efficiency improvement to 7.75% when compared with the device consisted of semiconductor absorber–metal contact. The study in the n–n type solar cell is expected to bring about more versatile materials utility, new interfacial engineering strategy and fundamental findings in the photovoltaic energy conversion process.

Keywords: n–n junction, carrier separation, solar cell, antimony selenosulfide, thin film

PACS: 88.40.hj, 78.67.Qa, 73.40.−c, 81.20.−n **DOI:** 10.1088/1674-1056/ac4022

1. Introduction

Solar cells convert light directly into electricity.[1] In the device operation, the absorber materials harvest light to generate either electron–hole pairs or excitons.[2,3] In any case, the separation of opposite charge carriers is enabled by a junction, either homojunction or heterojunction.[4,5] Conventionally, the efficient separation is conducted by the semiconductor with different conductivity types, i.e., p- and n-type semiconductors, since which generates an internal electric field within the p–n junction.[6–8] In fact, the high efficiency solar devices usually rely on the p–n junction.[9–15]

In this study, we demonstrate a device configuration based on n–n type inorganic semiconductor heterojunction, where $Sb_2(S,Se)_3$ and Sb_2Se_3 are applied as absorber and interfacial materials, respectively. Both the optical and electrical characterizations indicate n-type conductivity of the as-synthesized $Sb_2(S,Se)_3$ and Sb_2Se_3 films. Interestingly, $Sb_2(S,Se)_3$ and Sb_2Se_3 form a heterojunction, instead of the formation of gradient light harvesting layer. This n–n type heterojunciton is found to generate highly efficient carrier separation and in turn high power conversion efficiency (PCE).

2. Experiments

The FTO glass was ultrasonically cleaned with deionized water, isopropyl alcohol, acetone and ethanol for 30 min respectively. It was cleaned by ultraviolet ozone for 15 min to remove residual organic species. The CdS buffer layer was grown on the FTO substrate about 60 nm by the chemical bath deposition (CBD) method (66 °C, 16 min). The solution contains cadmium nitrate ($Cd(NO_3)_2$), thiourea (CH_4N_2S), and ammonia ($NH_3{\cdot}H_2O$) with concentrations of 0.15 mol·L^{-1}, 1.50 mol·L^{-1}, and 1.56 mol·L^{-1}, respectively. Afterwards, the sample was taken out and cleaned with water and alcohol and dried with nitrogen. Finally, the CdS film was treated by spin-coating of cadmium chloride ($CdCl_2$) methanol solution (20 mg·mL^{-1}) at 4000 rpm for 30 s and annealed (400 °C, 10 min) in air. The samples were cooled down naturally to room temperature.

Deposition of the $Sb_2(S,Se)_3$ and Sb_2Se_3 layer The $Sb_2(S,Se)_3$ absorber layer was deposited by hydrothermal deposition according to our reported method.[16] The Sb_2Se_3 was deposited on $Sb_2(S,Se)_3$ absorption layer via thermal evaporation under 10^{-4} Pa about 150 nm, where there are two evaporation sources. After the deposition of Sb_2Se_3, another evaporation source was used to evaporate the Se film about 20 nm on the Sb_2Se_3 surface. The samples were then transferred to a nitrogen glove box and annealed on a heating plate at 175 °C for 30 min.

Fabrication of solar cell devices Au electrode was deposited onto the $Sb_2(S,Se)_3$ or Sb_2Se_3 layer under a pressure of 5.0×10^{-4} Pa to complete the device fabrication. The effective area of the device was defined as 0.12 cm^2 and the photovoltaic performance measurement was conducted using a mask with an area of 0.04 cm^2.

†Corresponding author. E-mail: tchenmse@ustc.edu.cn

© 2022 Chinese Physical Society and IOP Publishing Ltd

Characterizations and measurements The surface and cross-section scanning electron microscopy were taken by the cold field-emission SEM (SU8200). The x-ray diffraction (XRD) of the samples was tested via the Bruker Advance D8 diffractometer (Cu, $K\alpha$, λ =1.5406 Å). The ultraviolet photoelectron spectroscopy (UPS) was measured through Thermo Scientific K-Alpha^{+}. The ultraviolet–visible absorption spectra were obtained by the ultraviolet–visible spectrophotometer (UV-vis DRS, SOLID 3700). Meanwhile, the capacitance–voltage (C–V) curves were obtained from the same electrochemical workstation with a frequency of 50 kHz and the AC amplitude of 5 mV. The devices were tested using a Keithley 2400 source-measure unit under AM 1.5 G. The external quantum efficiency (EQE) was measured using a single source illumination system (halogen lamp) combined with a monochromator. The EQE values of the devices were measured using an illumination system with a single source (halogen lamp) in connection with a monochromator (Model SPIEQ. 200). Optical deep-level transient spectroscopy (ODLTS) measurement was performed to detect the defects of the devices using a Phystech FT-1230 HERA DLTS system equipped with a 10 mW laser with a 635 nm wavelength. The capacitance was measured using a Boonton 7200 capacitance meter with an upper limit frequency of 1 MHz. In the actual process to record the ODLTS spectra of the solar cell devices, the frequency was varied in a range of 1 Hz to 75 kHz to measure the capacitance. The samples were placed in a liquid helium cryostat with a temperature scan ranging from 120 K to 425 K at 2 K intervals. The reverse bias, optical pulse width, and period width were 0.3 V, 10 ms, and 100 ms, respectively.

3. Results and discussion

In specific, the $Sb_2(S,Se)_3$ thin film was fabricated by the hydrothermal deposition method onto a CdS substate, which generated flat, compact surface morphology (Figs. 1(a) and 1(b)), this film is labeled as SbSSe film for the convenience of presentation.[16] The atomic ratio of S/(S+Se) is measured as 0.68 (Fig. S1). Afterwards, the Sb_2Se_3 film was fabricated by thermal evaporation deposition, this approach allows the generation of flat surface morphology onto the $Sb_2(S,Se)_3$ film with high surface coverage (Fig. 1(c)). The thicknesses of $Sb_2(S,Se)_3$ and Sb_2Se_3 in the optimized device are 250 nm and 150 nm, respectively (Fig. 1(a)).

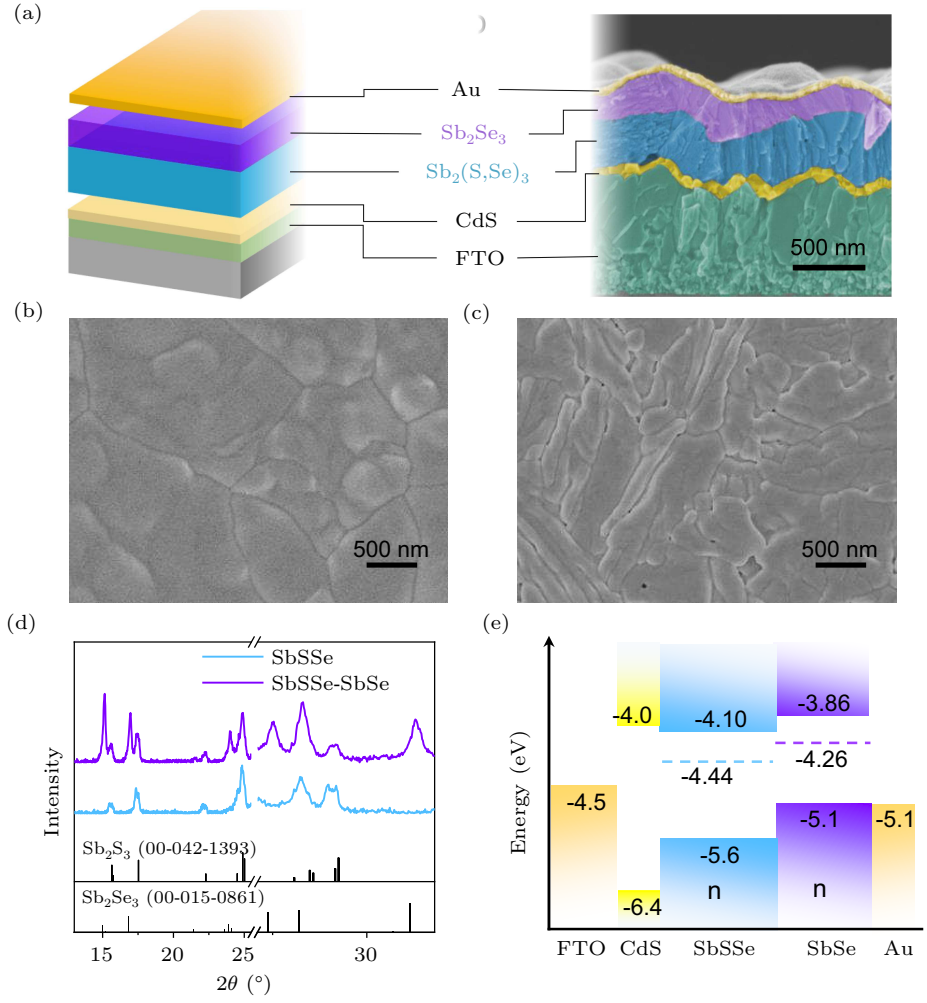


Fig. 1. (a) Schematic illustration of the device structure and SEM cross section of a typical device, (b) SEM image of the as-synthesized $Sb_2(S,Se)_3$ film, (c) SEM image of the as-synthesized Sb_2Se_3 film onto the surface of $Sb_2(S,Se)_3$, (d) XRD patterns of the $Sb_2(S,Se)_3$ and Sb_2Se_3 films, (e) energy level alignment of each layer in the device. The $Sb_2(S,Se)_3$ and Sb_2Se_3 are abbriviated as SbSSe and SbSe, respectively.

XRD characterization was firstly applied to determine the crystal structure of the as-obtained film (Fig. 1(d)). Both the $Sb_2(S,Se)_3$ and Sb_2Se_3 display similar diffraction patterns. The diffractions at 15.508°, 17.368°, 24.848°, 28.228° and 28.948° can be indexed as (020), (120), (130), (230) and (211) of stibnite crystal structures. In addition, there is a slight peak shifting towards low diffraction angle, owing to the larger atomic radius of Se than that of S. Furthermore, because of the presence of Sb_2Se_3 film, this film (denoted as SbSSe-SbSe film) exhibits diffraction peaks of both Sb_2Se_3 and $Sb_2(S,Se)_3$. The light absorption spectra show that the corresponding bandgaps of $Sb_2(S,Se)_3$ and Sb_2Se_3 are 1.50 eV and 1.24 eV, respectively (Figs. S2(a) and S2(b)).

We then measured the energy level of the as-synthesized film by ultraviolet photoelectron spectroscopy (UPS) (Figs. S2(c) and S2(b)). The valence band edge (VBE) and Fermi level (E_F) of $Sb_2(S,Se)_3$ are obtained as −5.6 eV and −4.44 eV, respectively. For Sb_2Se_3, the VBE and E_F are respectively changed to −5.1 eV and −4.26 eV. Combining with the bandgap value measured from the light absorption spectra, the conduction band edges are −4.10 eV and −3.86 eV for $Sb_2(S,Se)_3$ and Sb_2Se_3, respectively. In this regard, we are able to depict the energy alignment of the interfacial and absorber materials in the device (Fig. 1(e)). Clearly, the Fermi levels are much closer to the conduction band in both $Sb_2(S,Se)_3$ and Sb_2Se_3. We can readily conclude that both of the $Sb_2(S,Se)_3$ and Sb_2Se_3 display n-type conductivity.

We fabricated a complete device based on the above films to examine the photovoltaic performance. The control device was fabricated by depositing Au film directly onto the $Sb_2(S,Se)_3$ surface, forming FTO/CdS/$Sb_2(S,Se)_3$/Au device structure, abbreviated as SbSSe device. Figure 2(a) shows the current density–voltage (J–V) characteristic curves of the best performing device under standard one Sun (AM 1.5 G, 100 mW·cm^{-2}) illumination. The control device appears S-shape J–V curve, which may be due to the influence of the large valence band offset or surface defect states of $Sb_2(S,Se)_3$. The barrier formed between $Sb_2(S,Se)_3$ and Au electrode affects the charge transfer.[17,18] The corresponding J–V parameters are summarized in Table S1. The control device delivers a PCE of 4.86% with open-circuit voltage (V_{OC}) of 0.517 V, short-circuit current density (J_{SC}) of 18.19 mA/cm^2, and fill factor (FF) of 51.07%. After the deposition of Sb_2Se_3, it forms FTO/CdS/$Sb_2(S,Se)_3$/Sb_2Se_3/Au structure and is denoted as SbSSe-SbSe device. The PCE is strikingly increased to 7.75%, where the V_{OC}, J_{SC} and FF are 0.647 V, 18.46 mA/cm^2 and 64.86%, respectively. The V_{OC} and FF show essential improvement. The n–n type heterojunction was also demonstrated in organic solar cells and showed efficiency of 3%,[19] here the utilization of inorganic absorber and interfacial materials is promising for further improving the device performance.

In the control device, the difference between the E_F of Au electrode and the valence band edge (E_V) for $Sb_2(S,Se)_3$ is 0.5 eV (Fig. 1(e)), such a large energy offset is not conducive to hole extraction. However, the E_V of Sb_2Se_3 in the SbSSe-SbSe device is 0.5 eV higher than that of the control device (Fig. 1(e)), which is closer to the work function of Au. This energy alignment enables more efficient carrier transport, rendering the FF enhancement.

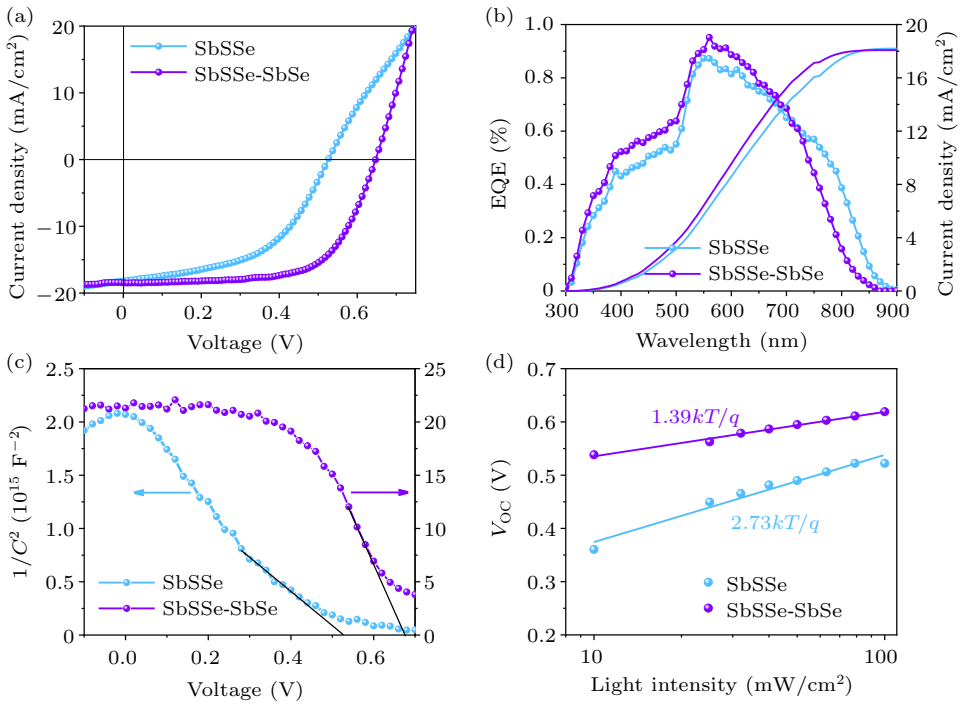


Fig. 2. (a) The J–V curves, (b) EQE, (c) C–V, and (e) light intensity dependent V_{OC} of the SbSSe and SbSSe-SbSe devices.

In the SbSSe device, obviously, the charge separation should be due to the extraction of Au electrode. In the SbSSe-SbSe solar cell, one can also consider that the $Sb_2(S,Se)_3/Sb_2Se_3$/Au semiconductor–metal contact is at work for the carrier separation, where a gradient $Sb_2(S,Se)_3/Sb_2Se_3$ absorber facilitates the carrier transport. The formation of gradient absorber would enhance the carrier transport for high FF. At the same time, this gradient band structure would result in reduced V_{OC} due to the lowered bandgap. However, the fact is that the V_{OC} exhibits essential increase from 0.517 V to 0.647 V. This contradiction implies new operational mechanism of the SbSSe-SbSe device. In this regard, we characterize the EQE of the devices (Fig. 2(b)). Surprisingly, both of the devices display nearly identical onset wavelength at $\sim$ 850 nm, in accordance with the spectral response of the $Sb_2(S,Se)_3$ film. If the absorber material of the device is $Sb_2(S,Se)_3/Sb_2Se_3$, the onset wavelength should be extended to $>$ 1000 nm since the band gap of Sb_2Se_3 is 1.2 eV. In fact, there is no red shift in the response spectrum of the SbSSe-SbSe solar cell. In this case, the Sb_2Se_3 layer was post-annealed at low temperature (175 °C), this annealing process is not able to generate crystalline Sb_2Se_3 for serving as light harvesting material. Instead, it plays a role as interfacial material. Therefore, on the ground of the changes in V_{OC} and EQE, we conclude that the Sb_2Se_3 facilitates the formation of n–n type heterojunction where $Sb_2(S,Se)_3$ serves as the light-harvesting material.

A possible process of electron and hole transport is shown in Fig. 3. For the SbSSe device, $Sb_2(S,Se)_3$/Au forms Ohmic contact (Fig. 3(a)), the carrier separation is enabled by the work function difference in the two electrodes.[19] For the SbSSe-SbSe device, the Fermi level alignment between $Sb_2(S,Se)_3$ and Sb_2Se_3 would form an electric field, which facilitates the carrier separation and transport and impedes the interface recombination (Fig. 3(b)).

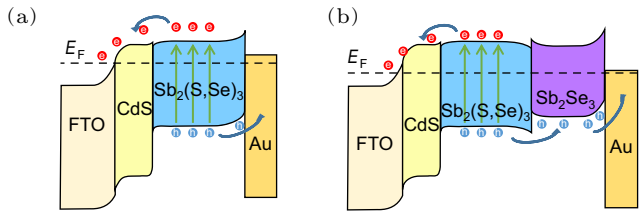


Fig. 3. The schematic illustration of the electron and hole transport in (a) SbSSe and (b) SbSSe-SbSe devices.

To examine the heterojunction quality of the device, capacitance–voltage (C–V) profiling was measured at room temperature and the frequency of 50 kHz in dark condition (Fig. 2(c)). The V_{bi} of the devices can be estimated by the point where the straight extension of the descending part of the curve intersects the X-axis. The V_{bi} of the SbSSe control device and SbSSe-SbSe device are 0.527 V and 0.676 V, respectively. This result is in good agreement with the V_{OC} changes, indicating that the n–n heterojunction between $Sb_2(S,Se)_3$ and Sb_2Se_3 increases the internal electrical field.

Furthermore, to analyze how the junction influences the recombination kinetics of two devices under working conditions, the relationship between V_{OC} and light intensity (I) was tested (Fig. 2(d)), in which the V_{OC} and logarithm of I satisfy the equation[20,21]

$$V_{OC} = \frac{\varepsilon kT \ln(I)}{q} + B, \tag{1}$$

where ε, k, T, q and B represent the ideal factor, Boltzmann constant, absolute temperature, fundamental charge and constant, respectively. Fitting the lines of $\ln(I)$ and V_{OC}, we can get the slope $\varepsilon kT/q$. Compared to the control device ($2.73kT/q$), the SbSSe-SbSe device shows the smaller slope ($1.39kT/q$), which indicates that the n–n type heterojunction can also alleviate the trap-assisted recombination under lighting condition.

To understand how the formation of n–n type junction influences the defect properties of the absorber materials in the device, we conducted deep level transient spectroscopy (DLTS) analysis (Fig. 4(a)). DLTS is a powerful tool for detecting the defect level, type and concentration in photovoltaic devices.[22,23] A voltage or light pulse is applied to fill the device trap and change the relevant capacitance. The transient capacitance is monitored under different temperatures, which exhibits the charge state at the deep level defect center. It should be pointed out that the signal of DLTS is seriously distorted in the FTO/CdS/$Sb_2(S,Se)_3$/Au device (Fig. S3), so that the result is not valid, due to the abrupt energy barrier between $Sb_2(S,Se)_3$ and Au.[24,25] Instead, a conventional Spiro-OMeTAD hole transporting material based SbSSe device (i.e., FTO/CdS/$Sb_2(S,Se)_3$/Spiro-OMeTAD/Au) is used here as a comparison. According to this characterization and Arrhenius plots (Fig. 4(b)), the absorber materials display n-type conductivity.

The defect energy level, concentrations (N_T), and cross-sections (σ) are calculated and summarized in Table S2. Obviously, the two devices exhibit different types of defects. There are three kinds of electron trap states detected in the n–n heterojunction-based device, which are denoted as E1, E2, and E3 (donor defects), respectively. The corresponding energy levels (E_T) are 0.237 eV, 0.560 eV and 0.774 eV below the conduction band edge (CBE). The energy level alignment (Fig. 4(d)) shows that trap E1 is less than 0.3 eV away from CBE and away from E_F, so it is not a major defect deteriorating the device efficiency.[23] In this case, the E2 and E3 are detrimental defects in the device. The $Sb_2(S,Se)_3$/Spiro-OMeTAD based device, on the other hand, exhibits two hole traps which are denoted as H1 and H2 (acceptor defects) with energy levels of 0.465 eV and 0.699 eV above the VBM (Fig. 4(c)).

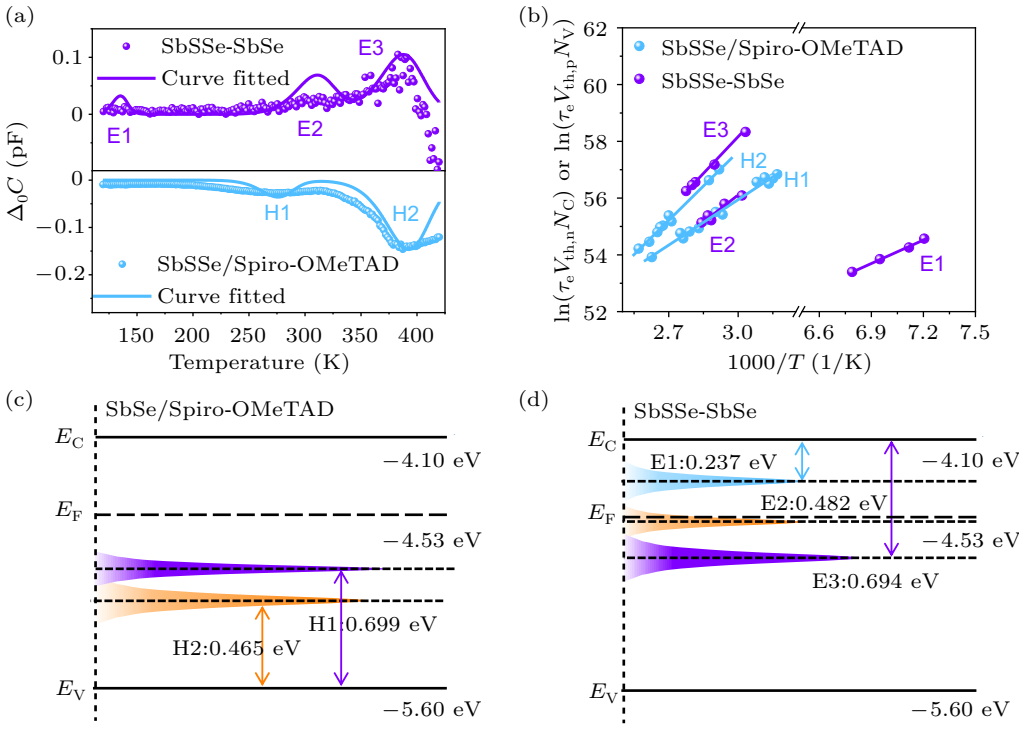


Fig. 4. (a) O-DLTS signals from SbSSe and SbSSe-SbSe devices, (b) Arrhenius plots obtained from O-DLTS signals. (c)–(d) Schematic diagrams of the defect energy levels of the absorber materials.

Both of them are deep-level defects. Furthermore, there is no significant difference of capture cross-section σ in both devices. However, the trap density (N_T) in SbSSe-SbSe device is essentially lower than that in $Sb_2(S,Se)_3$/Spiro-OMeTAD based device. Therefore, the SbSSe-SbSe device is less defective than that of the SbSSe device, although it exhibits one more defect type.

The fabrication of Sb_2Se_3 onto the surface of $Sb_2(S,Se)_3$ is through thermal deposition followed by a brief annealing in selenium vapor, this post-deposition and thermal treatment would induce the change in materials composition and defect properties. In addition, the fabrication of organic Spiro-OMeTAD hole transporting layer is via spin-coating approach with a mild annealing, which does not influence the absorber layer considerably.[16] In this case, the utilization of inorganic material possesses triple advantages: (1) facilitating the formation of optimized interface due to the identical crystal structure between $Sb_2(S,Se)_3$ and Sb_2Se_3, (2) forming junction that leads to more efficient carrier separation and transport and (3) modifying the defect properties of the pre-formed absorber layer.

4. Conclusion

In summary, we have demonstrated inorganic solar cells with n–n type heterojunction. We found that this device configuration is able to efficiently drive the carrier separation. Compared with semiconductor–metal contact, this n–n type heterojunction exhibits remarkably stronger capability of carrier separation and transport. This proof-of-concept study enables versatile materials utility, interfacial engineering as well as the defect manipulation. The study in the n–n type solar cell is also expected to bring about more fundamental findings in the photovoltaic energy conversion process.

Acknowledgments

Project supported by Institute of Energy, Hefei Comprehensive National Science Center (Grant No. 21KZS212), the National Key Research and Development Program of China (Grant No. 2019YFA0405600), the National Natural Science Foundation of China (Grant Nos. U19A2092 and 22005293), the China Postdoctoral Science Foundation (Grant No. 2021M693045), and Collaborative Innovation Program of Hefei Science Center, Chinese Academy of Sciences.

References

[1] Hovel H J 1975 *Solar Cells*, Vol. 11 of Semiconductors and Semimetals (New York: Academic Press) p. 2
[2] Green M A 1982 *Solar cells: Operating principles, technology and system applications* (Englewood Cliffs: Web) p. 2
[3] Granström M, Petritsch K, Arias A, Lux A, Andersson M R and Friend R 1998 *Nature* **395** 257
[4] Metzger W, Ahrenkiel R, Dashdorj J and Friedman D 2005 *Phys. Rev. B* **71** 035301
[5] Würfel U, Cuevas A and Würfel P 2014 *IEEE J. Photovolt.* **5** 461
[6] Hara K O and Usami N 2013 *J. Appl. Phys.* **114** 153101
[7] Kirchartz T, Bisquert J, Mora-Sero I and Garcia-Belmonte G 2015 *Phys. Chem. Chem. Phys.* **17** 4007
[8] Kabir I and Mahmood S A 2019 *Chin. Phys. B* **28** 128801
[9] Nakamura M, Yamaguchi K, Kimoto Y, Yasaki Y, Kato T and Sugimoto H 2019 *IEEE J. Photovolt.* **9** 1863

[10] Wang Y, Wu T, Barbaud J, Kong W, Cui D, Chen H, Yang X and Han L 2019 *Science* **365** 687
[11] Metzger W K, Grover S, Lu D, Colegrove E, Moseley J, Perkins C L, Li X, Mallick R, Zhang W, Malik R, Kephart J, Jiang C S, Kuciauskas D, Albin D S, Al-Jassim M M, Xiong G and Gloeckler M 2019 *Nat. Energy* **4** 837
[12] Yoshikawa K, Kawasaki H, Yoshida W, Irie T, Konishi K, Nakano K, Uto T, Adachi D, Kanematsu M, Uzu H and Yamamoto K 2017 *Nat. Energy* **2** 17032
[13] Peng S, Shi J, Pei, J, Liang Y, Cheng F, Liang J and Chen J 2009 *Nano Res.* **2** 484
[14] Mavlonov A, Razykovb T, Raziqa F, Gana J, Chantanac J, Kawanoc Y, Nishimurad T, Wei H, Zakutayev A, Minemotoc T, Zu X, Li S and Qiao L 2020 *Solar Energy* **201** 227
[15] Mavlonov A, Shukurov A, Raziq F, Mavlonov A, Shukurov A, Raziq F, Wei H, Kuchkarov K, Ergashev B, Razykov T and Qiao L 2020 *Solar Energy* **208** 451
[16] Tang R, Wang X, Lian W, Huang J, Wei Q, Huang M, Yin Y, Jiang C, Yang S, Xing G, Chen S, Zhu C, Hao X, Green M A and Chen T 2020 *Nat. Energy* **5** 587
[17] Chavali R V, De Wolf S and Alam M A 2018 *Prog. Photovolt.* **26** 241
[18] Chavali R V K, Wilcox, J R, Ray B, Gray J L and Alam M A 2014 *IEEE J. Photovolt.* **4** 763
[19] Song Q L, Yang H B, Gan Y, Gong C and Li M C 2010 *J. Am. Chem. Soc.* **132** 4554
[20] Yin X, Guan L, Yu J, Zhao D, Wang C, Shrestha N, Han Y, An Q, Zhou J, Zhou B, Yu Y, Grice C R, Awni R A, Zhang F, Wang J, Ellingson R J, Yan Y and Tang W 2017 *Nano Energy* **40** 163
[21] Duan J, Zhao Y, He B and Tang Q 2018 *Angew. Chem. Int. Ed.* **130** 3849
[22] Wen X, Chen C, Lu S, Li K, Kondrotas R, Zhao Y, Chen W, Gao L, Wang C, Zhang J, Niu G and Tang J 2018 *Nat. Commun.* **9** 2179
[23] Lian W, Jiang C, Yin Y, Tang R F, Li G, Zhang L, Che B and Chen T 2021 *Nat. Commun.* **12** 3260
[24] Toompuu J, Korolkov O, Sleptšuk N and Rang T 2010 *Elektron. Elektrotech.* **100** 51
[25] Noras J 1981 *Solid State Commun.* **39** 1225